Catalysis Today 165 (2011) 2–9

Contents lists available at ScienceDirect

Catalysis Today

journal homepage: www.elsevier.com/locate/cattod

The role of transition metal interfaces on the electronic transport in lithium–air batteries

Jingzhe Chen[a], Jens S. Hummelshøj[b], Kristian S. Thygesen[a], Jon S.G. Myrdal[a,c], Jens K. Nørskov[b,d], Tejs Vegge[c,*]

[a] Center for Atomic-scale Materials Design and Department of Physics, Technical University of Denmark, DK-2800 Lyngby, Denmark
[b] SUNCAT Center for Interface Science and Catalysis, SLAC National Accelerator Laboratory, Menlo Park, CA 94025, USA
[c] Materials Research Division, Risø National Laboratory for Sustainable Energy, Technical University of Denmark, DK-4000 Roskilde, Denmark
[d] Department of Chemical Engineering, Stanford University, Stanford, CA 94305, USA

ARTICLE INFO

Article history:
Received 30 September 2010
Received in revised form 3 December 2010
Accepted 6 December 2010
Available online 20 January 2011

Keywords:
Lithium–air batteries
Density functional theory
Electronic transport

ABSTRACT

Low electronic conduction is expected to be a main limiting factor in the performance of reversible lithium–air, Li–O_2, batteries. Here, we apply density functional theory and non-equilibrium Green's function calculations to determine the electronic transport through lithium peroxide, Li_2O_2, formed at the cathode during battery discharge. We find the transport to depend on the orientation and lattice matching of the insulator–metal interface in the presence of Au and Pt catalysts. Bulk lithium vacancies are found to be available and mobile under battery charging conditions, and found to pin the Fermi level at the top of the anti bonding peroxide $\pi^*(2p_x)$ and $\pi^*(2p_y)$ levels in the Li_2O_2 valence band. Under an applied bias, this can result in a reduced transmission, since the anti bonding $\sigma^*(2p_z)$ level in the Li_2O_2 conduction band is found to couple strongly to the metal substrate and create localized interface states with poor coupling to the Li_2O_2 bulk states. These observations provide a possible explanation for the higher overpotential observed for charging than discharge.

1. Introduction

The need for better and more sustainable methods for energy storage is growing rapidly, in particular in the energy and transportation sectors. New solutions and materials for high energy and power density storage are needed to solve the increasing demand for competitive (Hybrid) Electric Vehicles (H)EVs, where existing nickel metal hydride (used in the Toyota Prius) and lithium-ion (Tesla Roadster) battery technologies fall short on price, range, charge- and lifetime.

Since its commercialization in 1991 [1–3], the Li-ion battery has dominated the market for rechargeable batteries [4,5], but only small improvements have subsequently been made in terms of the energy capacity [6,7], and the best Li-ion batteries are currently storing ~300 mAh/g [8]. While materials like Si or Ge nanowires [9,10] and 3D-integrated all-solid-state battery concepts [11] could provide some improvements to Li-ion batteries, it is generally recognized that radically new approaches are needed for batteries to offer a real alternative to fossil fuels and to achieve consumer acceptance, i.e. improved reliability and safety, and most importantly, improvements in driving range and charge/discharge rates.

Li–O_2, generally referred to as Li–air, batteries with non-aqueous (aprotic) electrolytes were first demonstrated to be rechargeable in 1996 [12] by formation of Li_2O_2 during discharge. Although progress has recently been made [13–22], e.g. by addition of MnO_2 [5], Au [21] and Pt [22] catalysts, substantial improvements are still needed. The main challenges facing the Li–air battery is the limited electrical efficiency resulting from the overpotential/polarization losses at the cathode under charge and discharge [5], and the limited power and current densities currently achievable [23]. The overpotential is the difference between the equilibrium potential (U_0 = 2.96 V for Li/Li_2O_2) and the voltage during current-flowing conditions, i.e. the energy loss in the process, $\eta_{discharge} = U_0 - U_{discharge}$ and $\eta_{charge} = U_{charge} - U_0$, respectively.

A large asymmetry is also observed in the overpotentials for charge and discharge, i.e. a significantly higher potential is needed for charging, e.g. $U_{charge} \approx 4.5$ V and $U_{discharge} \approx 2.5$ V on a porous carbon electrode [24]; making the charging overpotential the most pertinent challenge to solve. We have previously proposed the initial step in the critical charging process to involve the formation of bound lithium superoxide species, LiO_2*, on the surface of Li_2O_2 [25]. These species form as a consequence of the creation of a lithium vacancy, V_{Li}, and subsequent transport of a lithium ion (Li^+) through the electrolyte and an electron (e^-) through Li_2O_2 to the electrode. We also showed that the presence of lithium vacancies in Li_2O_2 makes the otherwise insulating Li_2O_2 overlayer conduct-

* Corresponding author. Tel.: +45 4677 5818; fax: +45 4677 5758.
E-mail address: teve@risoe.dtu.dk (T. Vegge).

0920-5861/$ – see front matter © 2010 Elsevier B.V. All rights reserved.
doi:10.1016/j.cattod.2010.12.022

ing via holes in the valence band. For thin Li_2O_2 overlayers, surface vacancies are likely sufficient to obtain electronic conduction, but under high discharge rates, e.g. for automotive applications, where Li_2O_2 islands and thicker films are formed, either energetically expensive bulk lithium vacancies or other conduction channels, such as deposited Au-clusters [21], must be available to achieve electronic conduction.

Highly different conditions exist during charge and discharge, and the combined use of two distinctly different catalysts may be required, similar to the catalysts for Oxygen-Reduction-Reaction (ORR) [26,27] and Oxygen-Evolution-Reaction (OER) [28], respectively. Au has been shown to lower the overpotential for discharge [21] and recent experiments by Lu et al. [24] have shown Pt to lower the overpotential for charging dramatically, although at the cost of a reduced capacity. A bifunctional PtAu/C catalyst was also demonstrated [22] to retain the main properties of the two catalysts on charge and discharge, respectively. These results were obtained under optimized O_2-conditions and at low current densities, and the authors showed that the overpotentials grow significantly at increased currents. This effect is observed for both charge and discharge, although significantly more pronounced for the charging overpotential, where an increase of $\eta_{charge}(50\,mA/g) \approx 0.5\,V$ to $\eta_{charge}(250\,mA/g) \approx 1.0\,V$ is observed on the PtAu/C catalyst [22]. These observations underline the importance of obtaining a detailed understanding of the electronic conduction mechanisms at the insulator–catalyst interface.

Here, we apply non-equilibrium Green's function (NEGF) calculations [29] to determine the electronic transport through Li_2O_2 as well as Li_2O_2 deposited on the two promising transition metal catalysts, Au and Pt. This method has been used extensively to study quantum transport in a variety of different nano-scale systems including molecular junctions [30,31], atomic metal chains [32] and carbon nanotubes [33,34]. Here, we investigate the transport through Li_2O_2 grown on the close packed metal (1 1 1) facets, for the defect free interfaces as well as in the presence of lithium vacancies.

2. Theoretical methods

2.1. GPAW calculations

All calculations are performed within density functional theory [35,36] as implemented in the GPAW package [37,38] using the Atomic Simulation Environment [39] developed at the Technical University of Denmark. The GPAW package is a real space grid algorithm based on the projector augmented wavefunction method [40] with frozen core approximation. All calculations are spin polarized and performed using the RPBE exchange correlation functional [41]. All systems are sampled with a grid spacing of 0.2 Å and the slab systems (see Section 3) are sampled with a (2,2,1) k-point grid, while calculations of bulk metals are sampled using (8,8,8) k-points.

2.2. Non-equilibrium electron transport Green's function method

Finite bias electron transport calculations are performed using a localized LCAO basis set, i.e. linear combination of atomic orbitals, as implemented in GPAW [42]. Here, a central device region (C) is connected to two semi-infinite leads (L) and (R), e.g. Au(1 1 1) (L) and Li_2O_2(0 0 0 1) slabs (R) as seen in Fig. 1, which are kept at fixed electronic chemical potentials, μ_L and μ_R, to simulate an applied bias voltage of $V = (\mu_L - \mu_R)/e$ across the device region; in this case the Li_2O_2(0 0 0 1)@Au(1 1 1) interface (Fig. 1). As a consequence of the electronic screening, the electron potential inside the leads converges rapidly to the bulk value and sets the boundary conditions for the electrostatic potential inside C. Rather than obtaining the

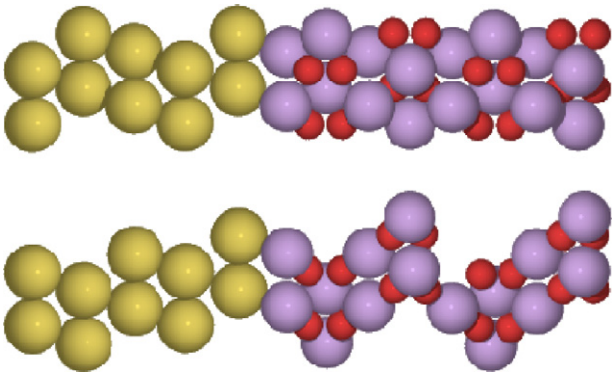

Fig. 1. The calculational setup for the scattering region for the Li_2O_2(0 0 0 1)@Au(1 1 1) (upper) and $Li_2O_2(0\,0\,0\,1)_{vac}$@Au(1 1 1) (lower) interfaces, i.e. the same interface with a Li-vacancy in the middle of the Li_2O_2 layer. The super cells contain 5 metal layers and 4 Li_2O_2 layers and 21 (upper) and 41 (lower) atoms in total.

wavefunctions from the eigenvalue equation we work with the Green's function (GF) of the central region defined by

$$G(E) = [ES - H_C - \Sigma_L(E) - \Sigma_R(E)]^{-1} \quad (1)$$

where S and H_C are, respectively, the overlap and Hamiltonian matrix of the central region in the LCAO basis. Note that we have suppressed the dependence on the bias voltage, V, in the above expression for notational simplicity. The self-energies, $\Sigma_{L/R}$, incorporate the open boundary conditions of the infinite bulk electrodes. We obtain the electron density, $n(r)$, by integrating the diagonal of the Green function, $G(r,r;E)$, along a contour in the complex energy plane. The Poisson equation is solved on the real-space grid to obtain the electrostatic contribution to the effective potential, $v(r)$, in region C. The boundary conditions for the Poisson equation at the C–L and C–R interfaces are given by the bulk potential of the leads (shifted by the applied bias voltage $\pm eV/2$), while periodic boundary conditions are used in the plane perpendicular to the direction of transport. The cycle $G \rightarrow n(r) \rightarrow v(r) \rightarrow H_C \rightarrow G$ is iterated until self-consistency using Pulay density mixing [43]. At self-consistency the elastic transmission function is calculated from [38,44]

$$T(E;V) = \mathrm{Tr}[G(E)\Gamma_L(E)G(E)^{\dagger}\Gamma_R(E)] \quad (2)$$

where $\Gamma_{L/R}(E) = i(\Sigma_{L/R}(E) - \Sigma_{L/R}(E)^{\dagger})$ and the trace is taken over the central region basis functions. In physical terms $T(E;V)$ gives the transmission probability for an electron incident on the interface with an energy E under an applied bias V. Finally, the current *per unit cell* is obtained from

$$I(V) = G_0 \int_{\mu_L}^{\mu_R} T(E;V)dE \quad (3)$$

where $G_0 = 2e^2/h$ is the quantum unit of conductance and corresponds to a resistance of 12.9 kΩ.

2.3. Reaction pathways and defect mobility

To analyze the mobility of the lithium vacancies, we determine the minimum energy path and energy barriers using the nudged elastic band NEB method [45,46]. We then determine the thermally activated reaction rates, $r(T)$, within harmonic transition state theory (hTST) [47,48], using the ground state activation energy, E_a, and the vibrational frequencies at the initial (ν_{IS}) and saddle points (ν_{TS}):

$$r(T) = \nu\,\mathrm{Exp}\left(-\frac{E_a}{k_B T}\right) = \left(\frac{\Pi\nu_{IS}}{\Pi\nu'_{TS}}\right)\mathrm{Exp}\left(-\frac{E_a}{k_B T}\right) \quad (4)$$

The vibrational frequencies are obtained using a finite difference approximation of the Hessian matrix with back and forward displacements of 0.01 Å. The prime indicates that the imaginary frequency corresponding to the reaction coordinate is omitted.

3. Calculational setup

To investigate the influence of transition metals on the electronic transport during charge and discharge conditions, we have investigated the following three systems: (a) Li_2O_2, (b) Li_2O_2(0 0 0 1)@Au(1 1 1) and (c) Li_2O_2(0 0 0 1)@Pt(1 1 1). The super cell slabs contain 21 atoms separated by 9–19 Å vacuum layers and the systems are modeled by 4 layers of Li_2O_2 on top of 5 metal layers using the lattice constants of the metals as retrieved from optimizations of the bulk metals (see Fig. 1); the bulk calculations use an orthorhombic super cell of 4 atoms to represent the fcc lattice. The slabs are optimized internally by keeping the two lowest metal layers in their bulk positions and relaxing the remaining atoms to a total force below 0.05 eV/Å. Lithium vacancies are modeled by removing a Li atom from a double super cell and relaxing the system internally; the resulting system has 41 atoms and half of the Li atoms in one of the 8 Li layers are removed, corresponding to a total vacancy concentration [V_{Li}] of 6.25%.

For the transport calculations, the central region (C) describing the metal–Li_2O_2 interface also contains 5 layers of metal and 4 layers of Li_2O_2. We have verified that this is sufficient to achieve convergence of the current and potential drop across the interface. The electrode regions, i.e. bulk metal and Li_2O_2, are calculated with normal DFT with periodical boundary conditions. We used a (6,2,1) *k*-point sampling for the NEGF self-consistent loop and a (12,4,1) *k*-point grid for evaluating the current. The PBE functional [49] is used for exchange-correlation, and an LCAO basis set corresponding to single-zeta plus polarization is adopted for all atomic species. We have verified that the results are converged with respect to the size of the LCAO basis set.

In the finite bias calculations, a positive bias is defined as sending electrons from the left to the right, i.e. in the case of Li_2O_2(0 0 0 1)@Au(1 1 1), Fig. 1, sending electrons from the metal to Li_2O_2,corresponding to battery discharge ($2Li^+ + 2e^- + O_2 \rightarrow Li_2O_2$); negative bias then corresponds to battery recharge.

4. Results and discussion

In our analysis of the electronic transport, we have focused on the electrode/catalyst interface in the steady state situation where the first layers of Li_2O_2 are already formed; corresponding to the situation following the initial discharge or under charging conditions. In this study, we do not include possible effects at the Li_2O_2–electrolyte interface.

We have previously determined the free energies of the reaction intermediates on a stepped $Li_2O_2(1-\bar{1}\,0\,0)$ surface [25], and by correcting for a small error in the applied Li_{BCC} formation energy, we find a heat of formation of Li_2O_2 of $\Delta H = -5.92$ eV (free energy of formation of $\Delta G = -5.28$ eV) as compared to experimental values of $\Delta H = -6.56$ eV and $\Delta G = -5.91$ eV, respectively [50]. The calculated equilibrium potential is thus $U_0 = -\Delta G/2e = 2.64$ V compared to 2.96 V from experiments. During discharge, all steps remain downhill in free energy until a potential of $U_{discharge} = \min[-\Delta G_i/e] = 2.26$ V is reached, yielding an overpotential for discharge of $\eta_{discharge} = U_0 - U_{discharge} = 0.38$ V. During charging, a potential of 3.32 V or higher is needed for all steps to be downhill in free energy, giving $U_{charge} = \max[-\Delta G_i/e] = 3.32$ V, and resulting in a charging overpotential of $\eta_{charge} = U_{charge} - U_0 = 0.68$ V, i.e. a 0.3 V asymmetry compared to $\eta_{discharge}$. For details on the free energy calculations, please refer to Ref. [25].

In the presence of transition metal catalysts, e.g. Au and Pt as investigated here and previously by Xu and Shelton [51], the Li_2O_2 discharge product can grow on the energetically preferred (1 1 1) metal facets, which both have a reasonable lattice match with to the (0 0 0 1) facet of Li_2O_2, i.e. $a_{Li_2O_2} = 3.22$ Å, $a_{Au} = 2.97$ Å and $a_{Pt} = 2.83$ Å, see Fig. 1. Other interfaces are also possible [52], and e.g. the lattice constant of the reconstructed $Li_2O_2(1-\bar{1}\,0\,0)$ facet, $c_{Li_2O_2(1-\bar{1}\,0\,0)} = 7.83$ Å, has a reasonable match with the 8.40 Å and 8.00 Å found for the (1 1 0) metal facets of Au and Pt, respectively. TEM experiments by Lu et al. [22] show the Au, Pt and PtAu nanoparticles, used in their Li–air experiments, to be dominated by (1 1 1) facets, favoring growth at this interface.

In the following, we show that the electronic transport depends on the specific orientation and lattice matching at the interface region, due to the alignment of the O_2^{2-} peroxide ion and its distance to the metal atoms. We find that pinning of the Fermi level by lithium vacancies at the top of the valence band of Li_2O_2 can lead to a lowering of the electronic transport across the interface, as a consequence of the creation of localized interface states.

4.1. Pure Li_2O_2

From the projected electronic density of states (PDOS) for Li_2O_2 (Fig. 2), it is seen that the conduction and valence bands are dominated by the oxygen 2p orbitals and show a strong resemblance to molecular O_2. Here, two neighboring lithium atoms have donated their 2*s* electrons to fill the empty states in the anti bonding $\pi^*(2p_x)$ and $\pi^*(2p_y)$ levels and form the peroxide ion, O_2^{2-}, causing an extension of the O–O bond from 1.24 Å to 1.56 Å. The conduction band is almost exclusively comprised of the oxygen $2p_z$ orbitals (see Fig. 2) forming the anti bonding $\sigma^*(2p_z)$ peroxide level. In contrast to the occupied $\pi^*(2p_x)$ and $\pi^*(2p_y)$ orbitals, the $\sigma^*(2p_z)$ orbital is aligned along the O–O axis.

As expected for GGA calculations, the band gap of bulk Li_2O_2 is substantially underestimated in GPAW, yielding a value of only 1.3 eV, compared to the 4.9 eV obtained with the more accurate GW calculations [25]. This underestimation of the band gap is likely to influence the absolute numbers for the onset potentials for electronic transmission, but the fundamental understanding and trends are still expected to hold. The absolute values of the determined onset potentials for charge and discharge can thus be expected to be correspondingly underestimated compared to experiments.

We have previously outlined the importance of lithium vacancies on the electronic conduction in bulk Li_2O_2 [25], where they were shown to pin the Fermi level at the top of the valence band (Fig. 2). Here, we see that the lithium vacancy induces a splitting of the conduction band into two separate bands around 2 and 4 eV.

We determine the V_{Li} formation energy to be 3.09 eV in the bulk for a low vacancy concentration of [V_{Li}] = 1/32 (3%), marginally lower (3.04 eV) at the 1/16 concentration used in the transport calculations and 3.00 eV in high concentration limit (1/8). The formation energy is slightly lower in the surface region, depending on the specific facet and site, and the value at the interface is likely to depend on the specific coordination to the metal. Although the absolute numbers may be sensitive to the concentration and specific configuration of the vacancies, this effectively means that for potentials $U_{charge} > 3.09$ V, there will be a thermodynamic driving force to create lithium vacancies. Using NEB calculations, we find the barrier for bulk V_{Li} migration to be 0.36 eV with a corresponding hTST prefactor of $\nu = 3.4 \times 10^{12}$ s^{-1}, resulting in a jump rate of $r = 3.6 \times 10^6$ s^{-1} (Eq. (4)) at room temperature. Recent experiments have shown a significant decrease in the capacity and output voltage of Li–air batteries when operated at lower temperatures [53], indicating the importance of thermally activated processes. The formation energy and barrier for V_{Li} mobility are, however, sufficiently

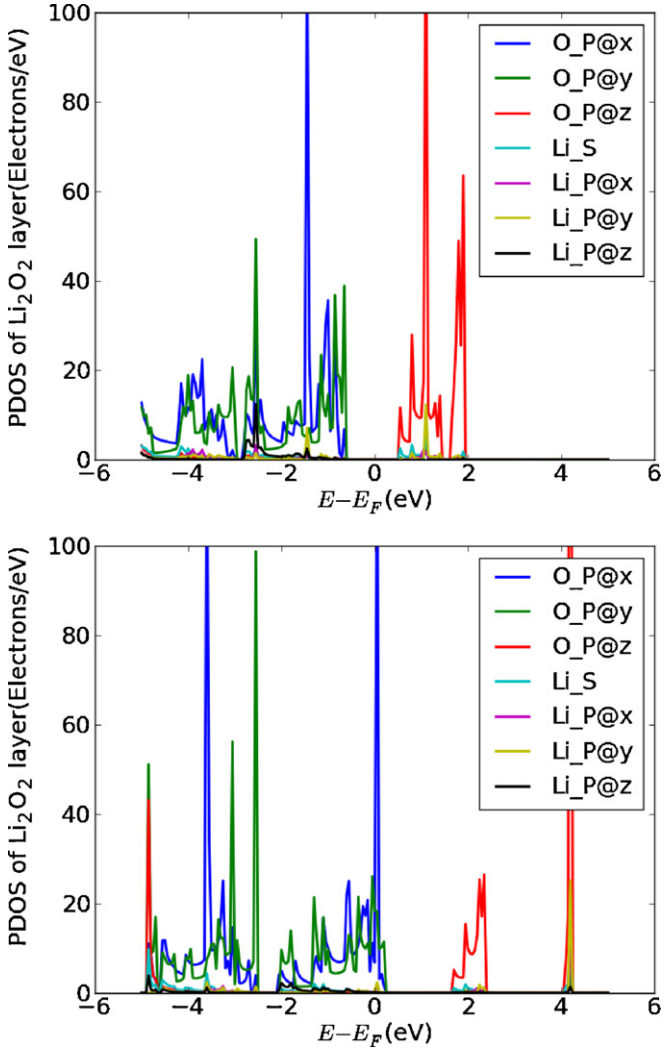

Fig. 2. The projected electronic density of states (PDOS) relative to the Fermi energy for bulk Li_2O_2 (upper) and bulk Li_2O_{2vac} (lower), i.e. bulk Li_2O_2 with a lithium vacancy. The top of the valence and conduction bands are seen to be dominated by the oxygen p orbitals, and bulk Li_2O_2 is found to have band gap of 1.3 eV. The lithium vacancy is seen to pin the Fermi level (dashed line) at the top of the valence band and induce a splitting of the conduction band and a corresponding up-shift in energy.

low to assume that under changing conditions, i.e. $U_{charge} > 3.5$ V, mobile bulk vacancies will expectedly be present and distributed throughout the Li_2O_2 layers. Whereas surface vacancies are likely to be present during discharge, $U_{discharge} < 2.8$ V, the bulk concentration is expected to be low.

Fig. 3 shows the calculated transmission coefficient at zero applied bias (0 V) for the vacancy free Li_2O_2 system (black) and the system containing a lithium vacancy (red). In the figure it is seen that transport is only possible in the presence of lithium vacancies (due to the band gap of the defect free system), where the Fermi level is pinned at the top of the valence band. In this case, the conduction occurs via the holes in valence band.

4.2. $Li_2O_2(0\,0\,0\,1)$@Au(1 1 1)

The relaxed $Li_2O_2(0\,0\,0\,1)$@Au(1 1 1) and $Li_2O_2(0\,0\,0\,1)_{vac}$@Au(1 1 1) interfaces are shown in Fig. 1. From the figure, it is seen the peroxide ions are aligned perpendicular to the interface region and located at distance of ~4.2 Å above the gold surface. The lithium vacancy is located in the middle of the Li_2O_2 part of the scattering region, thus creating a higher vacancy concentration (1/2) in one

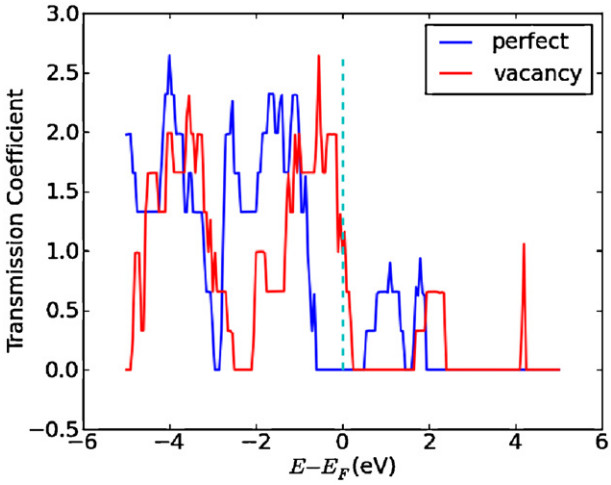

Fig. 3. Calculated transmission coefficients at zero bias (0 V) for bulk Li_2O_2 without lithium vacancies (blue) and with a lithium vacancy (red). The conductance is seen to be zero for the perfect system, but the presence of the lithium vacancy pins the Fermi level (dashed line) at the top of the valence band. (For interpretation of the references to color in this figure legend, the reader is referred to the web version of the article.)

lithium plane compared to the average value (1/16). This setup was chosen due to the requirements of the transport calculations, and in light of the limited sensitivity observed for the vacancy formation energy and PDOS, the obtained results are expected to be representative of different vacancy concentrations, although variations in the absolute currents are expected depending on the specific concentration and configuration of the vacancies.

The projected electronic density of states of the scattering region is shown in Fig. 4 for two different situations, i.e. the defect free $Li_2O_2(0\,0\,0\,1)$@Au(1 1 1) interface (upper), where the anti bonding $\sigma^*(2p_z)$ level is seen to be broadened compared to the bulk Li_2O_2 situation in Fig. 2 (upper), and the $Li_2O_2(0\,0\,0\,1)_{vac}$@Au(1 1 1) interface with a lithium vacancy (lower). For both systems, the top of valence band and the conduction band is seen to be dominated by the oxygen p orbitals. The lithium vacancy pins the Fermi level at the top of the anti bonding $\pi^*(2p_x)$ and $\pi^*(2p_y)$ peroxide levels in the valence band (lower), as seen for bulk Li_2O_{2vac}. The conduction band is also seen to split into an interface state at slightly lower energy, around 1–2 eV, and a bulk-like band, which has been shifted up in energy by an amount similar to that observed for the pinning in bulk Li_2O_2 (Fig. 2). The splitting is a consequence of the short spacial separation of the relevant molecular orbitals to the metal. Since the conduction band consists mainly of oxygen $2p_z$ orbitals (the anti bonding $\sigma^*(2p_z)$ peroxide level), which are aligned along the molecular axis, the coupling of the O_2^{2-} ions closest to the metal is so strong that they will follow the electronic chemical potential of the metal, μ_L, resulting in a weak coupling to the bulk-like Li_2O_2 states and thus a low electronic transport.

Since the formation energy of a lithium vacancy is below the minimum charging potential of $U_{charge} \geq 3.5$ V, such vacancies will be present during charging conditions and the charging currents should thus be evaluated in the presence of lithium vacancies. At discharge potentials, $U_{discharge} \leq 2.8$ V, the concentration of bulk lithium vacancies will be lower and the defect free scenario is likely to be applicable.

During the critical charging process (negative bias, V), the Fermi level in Au is lowered by $eV/2$ and correspondingly raised by $eV/2$ in Li_2O_2; causing electron transfer from Li_2O_2 to Au (Fig. 5). Due to the band gap in Li_2O_2 this will only be possible when the applied bias is sufficient to overcome the band gap and allow transfer from the conduction band of Li_2O_2. At a negative bias of −2 V, the PDOS for

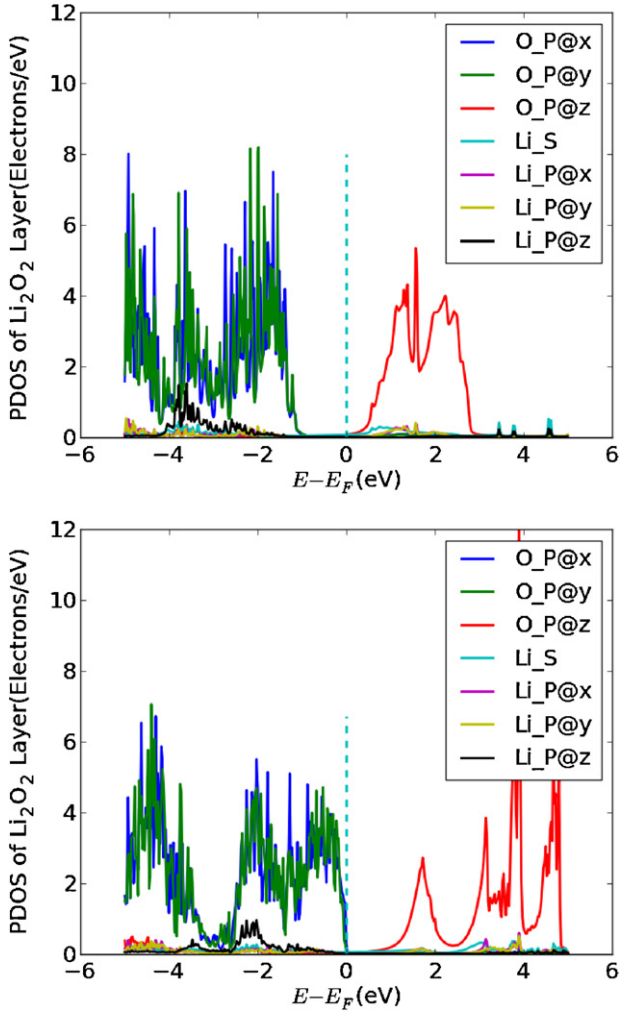

Fig. 4. The project electronic density of states (PDOS) relative to the Fermi energy for $Li_2O_2(0\,0\,0\,1)$@Au(1 1 1) (upper) shows a valence band dominated by oxygen the p_x and p_y orbitals and a conduction band which is dominated by oxygen p_z orbitals, separated by a band gap of 1.8 eV. In the PDOS for $Li_2O_2(0\,0\,0\,1)_{vac}$@Au(1 1 1) (lower), the lithium vacancy is seen to pin the Fermi level (dashed line) at the top of $\pi^*(2p_x)$ and $\pi^*(2p_y)$ level in the valance band and split the conduction band into a low energy interface state at 1–2 eV and a bulk-like band around 4 eV.

the vacancy system shows that the $\sigma^*(2p_z)$ interface state couples strongly to the metal and follows the electronic chemical potential of gold (μ_L). The $\pi^*(2p_x)$ and $\pi^*(2p_y)$ levels on the other hand follow the Fermi level in Li_2O_2. Looking at Fig. 2, there are no bulk states corresponding to the $\sigma^*(2p_z)$ interface state and hence there will be poor transport through this state.

Fig. 6 shows the calculated transmission curves for $Li_2O_2(0\,0\,0\,1)$@Au(1 1 1) (upper) and $Li_2O_2(0\,0\,0\,1)_{vac}$@Au(1 1 1) (lower) at three different bias potentials: 0 V (blue), 1 V (red) and 2 V (green); corresponding to three stages of the battery discharge. At zero bias (blue), the transmission is seen to be zero in both systems. At 1 V (red), the transmission peak is seen to be at the edge of the bias window for the defect free system giving a small transmission, but effectively zero for the system with a vacancy. At 2 V (green), the transmission peak in the conduction band of $Li_2O_2(0\,0\,0\,1)$@Au(1 1 1) (upper) is clearly within the bias window (dashed green lines), and resulting in significant transmission, whereas the $Li_2O_2(0\,0\,0\,1)_{vac}$@Au(1 1 1) (lower) system only has a limited transmission through the valence band. The conduction band transmission peak is seen to remain fixed in the perfect system, but shift with the Fermi level of Li_2O_2 for the vacancy system.

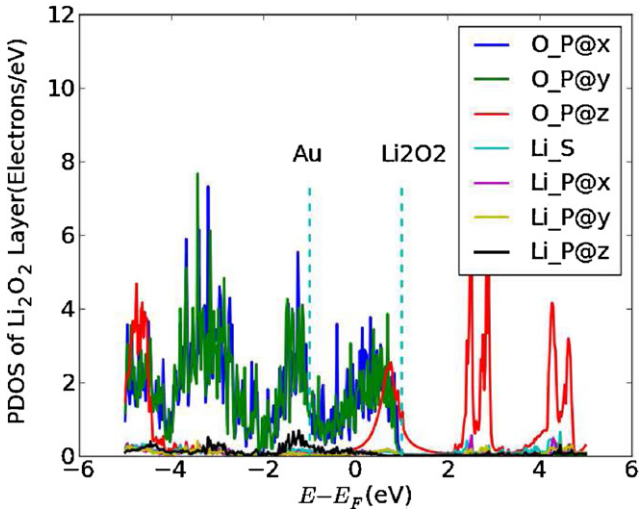

Fig. 5. The project density of states (PDOS) relative to the Fermi energy for $Li_2O_2(0\,0\,0\,1)_{vac}$@Au(1 1 1) at a negative bias of −2 V (charging conditions), where the Fermi level of Au is seen to be shifted down by 1 eV and correspondingly up by 1 eV for Li_2O_2 (dashed lines). The oxygen p_x and p_y orbitals are seen to follow the electronic chemical potential of Li_2O_2, whereas the localized p_z orbital follows the electronic chemical potential of Au. The bulk-like part of the p_z orbital couples primary to Li_2O_2 and remains outside the bias window.

Fig. 7 shows the equivalent transmission curves at 0 V (blue) as a reference and two negative bias potentials (charging): −1 V (red) and −2 V (green). At −1 V (red), a small transmission is possible through the valance band in the vacancy system and the conduction band peak is seen to be at the edge of the bias window (dashed red lines) for the perfect system. At −2 V (green), the transmission peak is in the bias window (dashed green lines) for the perfect system and resulting in significant transmission through the conduction band, whereas only a limited transmission is possible in the vacancy system.

4.3. $Li_2O_2(0\,0\,0\,1)$@Pt(1 1 1)

Identical calculations have been performed on the $Li_2O_2(0\,0\,0\,1)$@Pt(1 1 1) and $Li_2O_2(0\,0\,0\,1)_{vac}$@Pt(1 1 1) interfaces as for Au. The lattice constant of Pt is also found to have a good match with the $Li_2O_2(0\,0\,0\,1)$ surface, and the interface distances are comparable to those found for Au.

The calculated PDOS for the $Li_2O_2(0\,0\,0\,1)$@Pt(1 1 1) and $Li_2O_2(0\,0\,0\,1)_{vac}$@Pt(1 1 1) interfaces are shown in Fig. 8, and a strong resemblance to the gold interface is observed. Only a small difference is observed in the band gap, where 1.6 eV is found for the Pt(1 1 1) interface compared to 1.8 eV for the Au(1 1 1) interface. As for the PDOS, the calculated transmission coefficients at different bias potentials are also very similar to those obtained for Au and not shown here, since the main differences are well captured by the comparison of the IV curves presented in the following section.

4.4. Calculated IV curves

Fig. 9 shows the calculated IV curve for defect free $Li_2O_2(0\,0\,0\,1)$@Au(1 1 1) (blue) and $Li_2O_2(0\,0\,0\,1)$@Pt(1 1 1) (turquoise) systems. The conduction is found to be limited ($\sim 10^{-7}$ μA) at low bias (±0.2 V) for both systems. At onset potentials of around ±1 V, respectively, the current is seen to grow rapidly. A slight asymmetry is also observed, indicating a faster transport under charging than discharging conditions when no defects are present. Slightly lower onset potentials are seen for

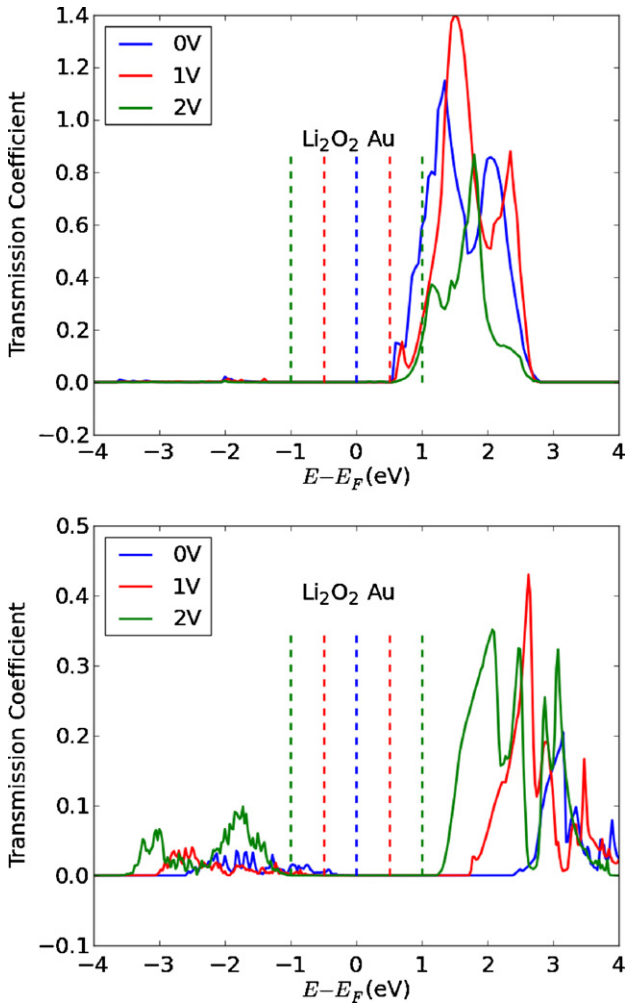

Fig. 6. Transmission curves for $Li_2O_2(0\,0\,0\,1)$@Au(1 1 1) (upper) and $Li_2O_2(0\,0\,0\,1)_{vac}$@Au(1 1 1) (lower) at three different bias potentials: 0 V (blue), 1 V (red) and 2 V (green); corresponding to three stages of the battery discharge. At zero bias (blue), the transmission is seen to be zero in both systems. At 1 V (red), the transmission peak is seen to be at the edge of the bias window (dashed red lines) for the defect free system, but effectively zero for the vacancy system. At 2 V (green), the transmission peak in the conduction band of $Li_2O_2(0\,0\,0\,1)$@Au(1 1 1) (upper) is in the bias window (dashed green lines) resulting in significant transmission, whereas the $Li_2O_2(0\,0\,0\,1)_{vac}$@Au(1 1 1) (lower) system only has a limited transmission through the valence band. The conduction band transmission peak is seen to remain fixed in the perfect system, but shift with the Fermi level (dashed lines) of Li_2O_2 for the vacancy system. (For interpretation of the references to color in this figure legend, the reader is referred to the web version of the article.)

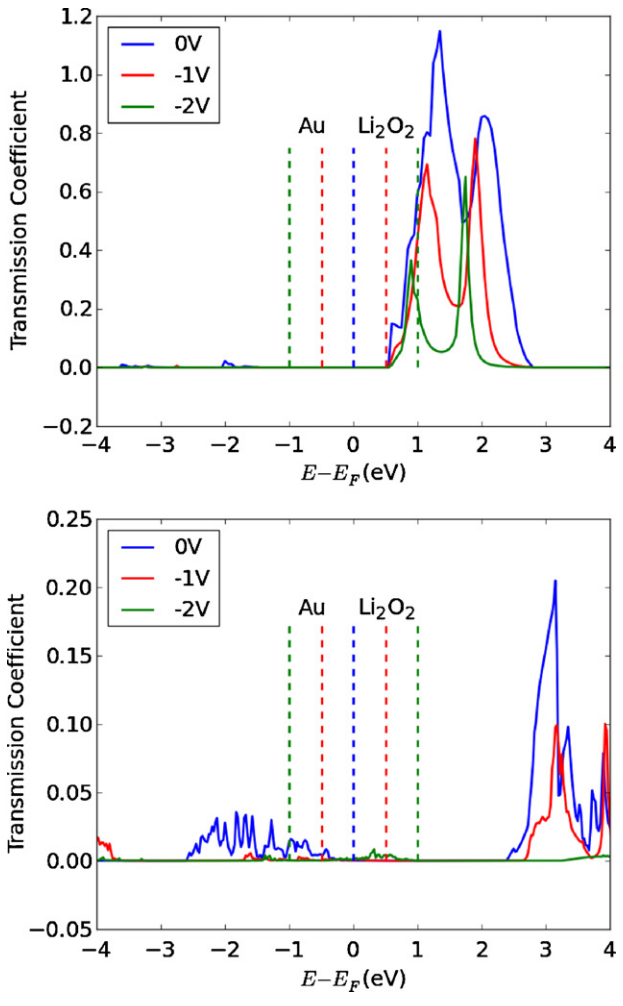

Fig. 7. Transmission curves for $Li_2O_2(0\,0\,0\,1)$@Au(1 1 1) (upper) and $Li_2O_2(0\,0\,0\,1)_{vac}$@Au(1 1 1) (lower) at three different bias potentials: 0 V (blue), −1 V (red) and −2 V (green); corresponding to three stages of the battery charge. At zero bias (blue), the transmission is seen to be zero in both systems. At −1 V (red) a small transmission is possible through valance band in the vacancy system and the conduction band peak is seen to be at the edge of the bias window (dashed red lines) for the perfect system. At −2 V (green), the transmission peak is in the bias window (dashed green lines) for the perfect system, resulting in significant transmission through the conduction band, whereas only a limited transmission is possible in the vacancy system. (For interpretation of the references to color in this figure legend, the reader is referred to the web version of the article.)

Pt than Au, which is a likely consequence of the smaller interface band gap.

Given the higher potentials needed for charging, part of the explanation for the experimentally observed asymmetry in the overpotentials for charging and discharging can be a result of bulk lithium vacancies being readily formed at charging potentials and highly mobile at room temperature, $r_{jump} = 3.6 \times 10^6\ s^{-1}$, in contrast to discharge conditions.

Fig. 10 shows the calculated IV curve for $Li_2O_2(0\,0\,0\,1)_{vac}$@Au(1 1 1) (red) and $Li_2O_2(0\,0\,0\,1)_{vac}$@Pt(1 1 1) (green) systems with lithium vacancies. The conduction is found to be limited but high ($\sim 10^{-4}$ μA) compared to the defect free interface at low bias (±0.2 V) for both systems. At an onset potential of around −0.5 V (charging), the current is seen to grow, whereas no increase is observed for discharge up to 2 V. The current is found to be highly asymmetric and the absolute currents during charging (negative bias) are found to be an order of magnitude below those for the defect free systems.

Under discharge conditions (without vacancies), a significantly higher current can be drawn on Au(1 1 1), $I_{Au(111)}(2\,V) = \sim 1.5\ \mu A$, compared to charging situation (with vacancies), where the current is roughly an order of magnitude lower, $I_{Au(1\,1\,1)\text{-}vac}(-2\,V) = -0.18\ \mu A$ (see Fig. 9). The situation is very similar on Pt(1 1 1), having a significantly higher discharge current (without vacancies), $I_{Pt(1\,1\,1)}(2\,V) = \sim 3.0\ \mu A$ than that observed under charging conditions, $I_{Pt(1\,1\,1)\text{-}vac}(-2\,V) = -0.17\ \mu A$ (with vacancies). Given the underestimation of the band gap in the calculation, the absolute values of the onset potentials are likely underestimated compared to experiments. Based on these results, the effect of the metal substrate is clear, and although the transport appears to be sensitive to the interface band gap, the observed differences between Au(1 1 1) and Pt(1 1 1) are within the uncertainty of the calculations; a good interface matching is, however, found to be important.

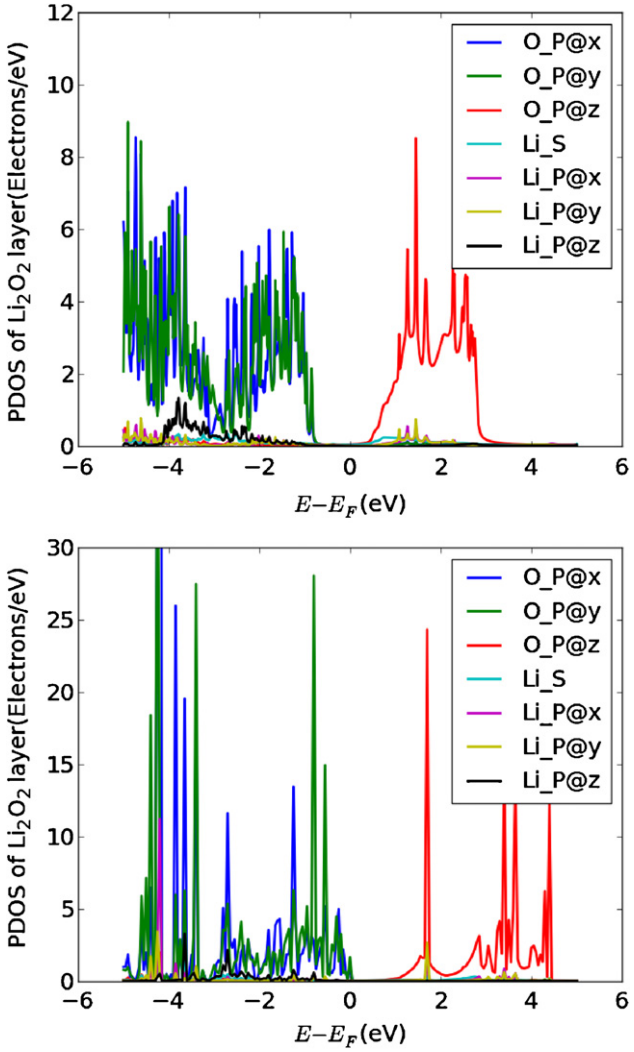

Fig. 8. The projected density of states (PDOS) relative to the Fermi energy for $Li_2O_2(0\,0\,0\,1)$@Pt(1 1 1) (upper) and $Li_2O_2(0\,0\,0\,1)_{vac}$@Pt(1 1 1) (lower). A band gap of 1.6 eV is found for the defect free interface, and the lithium vacancy is seen to pin the Fermi level (dashed line) at the top of the valance band of Li_2O_2.

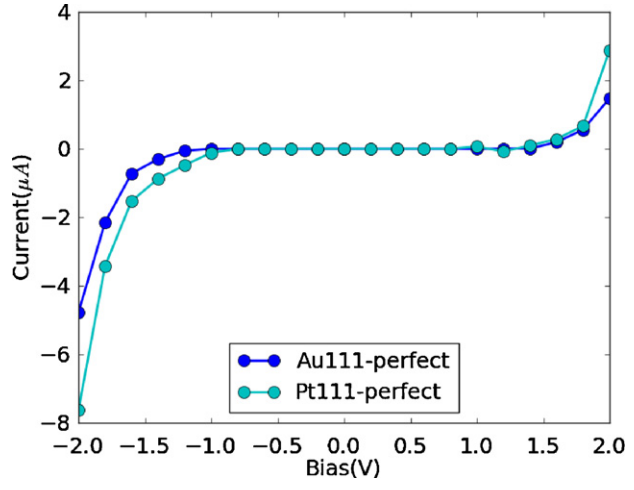

Fig. 9. Calculated IV curves for the defect free $Li_2O_2(0\,0\,0\,1)$@Au(1 1 1) (blue) and $Li_2O_2(0\,0\,0\,1)$@Pt(1 1 1) (turquoise) systems. The conduction is found to be limited ($\sim 10^{-7}$ μA) at low bias (±0.2 V) for both systems. At the onset potentials of around ±1 V, respectively, the current is seen to grow rapidly. A slight asymmetry is observed, indicating faster transport under charging conditions. Slightly lower onset potentials are seen for Pt than Au. (For interpretation of the references to color in this figure legend, the reader is referred to the web version of the article.)

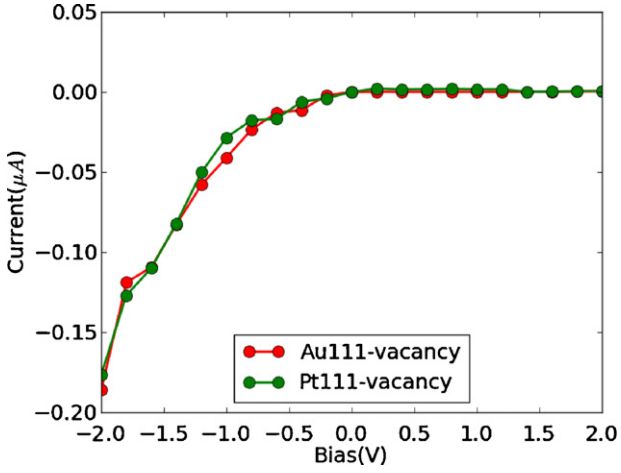

Fig. 10. Calculated IV curves for the $Li_2O_2(0\,0\,0\,1)_{vac}$@Au(1 1 1) (red) and $Li_2O_2(0\,0\,0\,1)_{vac}$@Pt(1 1 1) (green) systems with lithium vacancies. The conduction is found to be limited ($\sim 10^{-4}$ μA) at low bias (±0.2 V) for both systems. At the onset potential of around −0.5 V (charging), the current is seen to grow, whereas no increase is observed for discharge up to 2 V. The current is found to be highly asymmetric and the absolute currents during charging are found to be an order of magnitude below those for the defect free systems (see Fig. 9). (For interpretation of the references to color in this figure legend, the reader is referred to the web version of the article.)

Experiments clearly show a decrease in the overpotentials when operating at low currents, most pronounced for the charging overpotential (negative bias) [22], where we also see the lowest conduction when the lithium vacancies are introduced. It should also be noted that the absolute currents obtained at high bias in this study ($\sim 1\,\mu A/nm^2$ metal surface area) are significantly above those typically realized experimentally, e.g. $\sim 0.1\,mA/cm^2_{electrode}$ [24]. At low bias (±0.2 V), the absolute currents are significantly lower, e.g. $\sim 10^{-7}\,\mu A/nm^2_{metal\ surface}$ for $Li_2O_2(0\,0\,0\,1)$@Au(1 1 1) and $\sim 10^{-4}\,\mu A/nm^2_{metal\ surface}$ for the $Li_2O_2(0\,0\,0\,1)_{vac}$@Au(1 1 1) interface. This would correspond to a current of $\sim 10^{-4}\,mA/cm^2_{Au(1\,1\,1)\,surface}$ for the defect free system, and even when taking in to account that only a fraction of the electrode area consists of exposed (1 1 1) metal facets, the calculated currents are still significantly above those realized experimentally. It should also be noted that these numbers do not include the Li_2O_2–electrolyte interface, which may cause the transport to depend on the thickness of the Li_2O_2 layer, such that arbitrarily low currents can be obtained depending on the thickness. Such a dependence would also be consistent with the observed drops in the required overpotential in the later stages of charging (thin Li_2O_2 layers) as reported by Lu et al. on Pt and PtAu/C [22,24].

The calculated transport is also assumed to be coherent, but it is uncertain whether this approximation holds under experimental conditions, where electron–phonon coupling and polarons, morphological effects and interactions with the electrolyte are likely to important. The observed temperature dependence reported by Wilcke and co-worker [53] on the capacity and output voltage could be an indication of such interactions.

5. Conclusion

The electronic conduction is found to be sensitive to the orientation and lattice matching of the metal–insulator interface, and we show that the transport depends on the alignment of the O_2^{2-} peroxide ions in Li_2O_2 to the metal surface. The anti bonding interface $\sigma^*(2p_z)$ state in the conduction band couples strongly to the metal state and its electronic chemical potential (μ_L) in the $Li_2O_2(0\,0\,0\,1)$@Au(1 1 1) and $Li_2O_2(0\,0\,0\,1)$@Pt(1 1 1) interfaces.

Bulk lithium vacancies are found to be present under charging conditions and to pin the Fermi level at the top of the anti bonding peroxide $\pi^*(2p_x)$ and $\pi^*(2p_y)$ levels in the valence band of Li_2O_2. Under an applied bias, these states follow the electronic chemical potential of Li_2O_2 (μ_R), whereas the interface $\sigma^*(2p_z)$ states are aligned along the O–O bond and have a strong coupling to the metal states and follow its electronic chemical potential, resulting in a reduced transport during charging.

These observations lead to a possible explanation for the experimentally observed asymmetry in the overpotentials for battery charge and discharge, which may enhance the ~0.3 V asymmetry resulting from the formation of LiO_2^* species and the 4 electron process previously reported [25].

More work has to be done to understand the role of transition metal interfaces on the electronic transport in Li–air batteries. This includes a better understanding of the concentration of lithium and peroxide defects under different potentials, as well as other interfaces, e.g. the Li_2O_2(1 0 0)@Au(1 1 0) interface, where the O_2^{2-} ions are aligned parallel to the metal and the dependence of thickness of the Li_2O_2 layers and the effect of the Li_2O_2–electrolyte interface.

In addition to the electronic properties, a better understanding of the role of the electrolyte reactions in Li–air batteries is also required.

Acknowledgements

The authors would like to acknowledge the Danish Center for Scientific Computing, the Catalysis for Sustainable Energy (CASE) initiative and the Center of Atomic-Scale Materials Design (CAMD). CASE is funded by the Danish Ministry of Science, Technology and Innovation, and CAMD is funded by the Lundbeck Foundation. U.S. Department of Energy, Office of Basic Energy Sciences under Center on Nanostructuring for Efficient Energy Conversion (CNEEC) and Center for Interface Science and Catalysis – Sustainable energy through Catalysis (SUNCAT).

References

[1] K. Mizushima, P.C. Jones, P.J. Wiseman, J.B. Goodenough, Mater. Res. Bull. 15 (1980) 783.
[2] M.M. Thackeray, W.I.F. David, P.G. Bruce, J.B. Goodenough, Mater. Res. Bull. 18 (1983) 461.
[3] T. Nagaura, Prog. Batteries Solar Cells 10 (1991) 209.
[4] M.S. Whittingham, Chem. Rev. 104 (2004) 4271.
[5] T. Ogasawara, A. Débart, M. Holzapfel, P. Novák, P.G. Bruce, J. Am. Chem. Soc. 128 (2006) 1390.
[6] J.M. Tarascon, M. Armand, Nature 414 (2001) 359.
[7] A. Shukla, T.P. Kumar, Curr. Sci. 93 (2008) 314.
[8] M. Armand, J.M. Tarascon, Nature 451 (2008) 652.
[9] L.F. Cui, R. Ruffo, C.K. Chan, H. Peng, Y. Cui, Nano Lett. 9 (2009) 491.
[10] C.K. Chan, X.F. Zhang, Y. Cui, Nano Lett. 8 (2008) 307.
[11] L. Baggetto, R.A. Niessen, F. Roozeboom, P.H. Notten, Adv. Funct. Mater. 18 (2008) 1057.
[12] K.M. Abraham, Z. Jiang, J. Electrochem. Soc. 143 (1996) 1.
[13] J. Read, et al., J. Electrochem. Soc. 150 (2003) A1351.
[14] S.S. Zhang, D. Foster, J. Read, J. Power Sources 195 (2010) 1235.
[15] C.O. Laoire, S. Mukerjee, K.M. Abraham, E.J. Plichta, M.A. Hendrickson, J. Phys. Chem. C 113 (2009) 20134.
[16] B. Kumar, et al., J. Electrochem. Soc. 157 (2010) A50.
[17] P.G. Bruce, B. Scrosati, J.M. Tarascon, Angew. Chem. Int. Ed. Engl. 47 (2008) 2930.
[18] A. Debart, J. Bao, G. Armstrong, P.G. Bruce, ECS Trans. 3 (2007) 225.
[19] A. Débart, J. Bao, G. Armstrong, P.G. Bruce, J. Power Sources 174 (2007) 1177.
[20] J. Read, J. Electrochem. Soc. 153 (2006) A96.
[21] F.U. Renner, et al., Electrochim. Acta 53 (2008) 6064.
[22] Y.-C. Lu, Z. Xu, H.A. Gasteiger, JACS Commun. (2010), doi:10.1021/ja1036572.
[23] X.-h. Yang, Y.-y. Xia, J. Solid State Electrochem. 14 (2010) 109.
[24] Y.-C. Lu, Z. Xu, H.A. Gasteiger, M.C. Parent, V. Chiloyan, Y. Shao-Horn, Electrochem. Solid State Lett. 13 (2010) A69.
[25] J.S. Hummelshøj, et al., J. Chem. Phys. 132 (2010) 1.
[26] J. Greeley, J.K. Norskov, J. Phys. Chem. C 113 (2009) 4932.
[27] J. Greeley, et al., Nat. Chem. 1 (2009) 552.
[28] R. Forgie, G. Bugosh, K.C. Neyerlin, Z.C. Liu, P. Strasser, Electrochem. Solid State Lett. 13 (2010) D36.
[29] M. Brandbyge, J.L. Mozos, P. Ordejon, J. Taylor, K. Stokbro, Phys. Rev. B 65 (2002) 165401.
[30] D.J. Mowbray, G. Jones, K.S. Thygesen, J. Chem. Phys. 128 (2008) 111103.
[31] K.S. Thygesen, K.W. Jacobsen, Phys. Rev. Lett. 94 (2005) 036807.
[32] K.S. Thygesen, K.W. Jacobsen, Phys. Rev. Lett. 91 (2003) 146801.
[33] J.M. Garcia-Lastra, K.S. Thygesen, M. Strange, A. Rubio, Phys. Rev. Lett. 101 (2008) 236806.
[34] K.S. Thygesen, K.W. Jacobsen, Chem. Phys. 319 (2005) 111.
[35] P. Hohenberg, W. Kohn, Phys. Rev. B 136 (1964) B864.
[36] W. Kohn, L.J. Sham, Phys. Rev. 140 (1965) 1133.
[37] J.J. Mortensen, L.B. Hansen, K.W. Jacobsen, Phys. Rev. B 71 (2005) 035109.
[38] J. Enkovaara, et al., J. Phys.: Condens. Matter 22 (2010) 253202.
[39] S.R. Bahn, K.W. Jacobsen, Comp. Sci. Eng. 4 (2002) 56.
[40] P. Blöchl, Phys. Rev. B 50 (1994) 17953.
[41] B. Hammer, L.B. Hansen, J.K. Nørskov, Phys. Rev. B 59 (1999) 7413.
[42] A.H. Larsen, M. Vanin, J.J. Mortensen, K.S. Thygesen, K.W. Jacobsen, Phys. Rev. B 80 (2009) 195112.
[43] P. Pulay, Chem. Phys. Lett. 73 (1980) 393.
[44] Y. Meir, N. Wingreen, Phys. Rev. Lett. 68 (1992) 2512.
[45] G. Henkelman, H. Jonsson, J. Chem. Phys. 111 (1999) 7010.
[46] H. Jónsson, G. Mills, K.W. Jacobsen, Classical and Quantum Dynamics, in Condensed Phase Simulations, World Scientific, Singapore, 1998.
[47] P. Hänggi, P. Talkner, M. Borkovec, Rev. Mod. Phys. 62 (1990) 251.
[48] T. Vegge, T. Rasmussen, T. Leffers, O.B. Pedersen, K.W. Jacobsen, Phys. Rev. Lett 85 (2000) 3866.
[49] K. Burke, J.P. Perdew, Y. Wang, Phys. Rev. Lett. 77 (1996) 3865.
[50] M.W. Chase Jr., NIST-JANAF Thermochemical Tables, fourth edition, J. Phys. Chem. Ref. Data, Monograph 9 (1998) 1–1951.
[51] Y. Xu, W.A. Shelton, J. Chem. Phys. 133 (2009) 024703.
[52] N. Seriani, Nanotechnology 20 (2009) 445703.
[53] G. Girishkumar, B. McCloskey, A.C. Luntz, S. Swanson, W. Wilcke, J. Phys. Chem. Lett. 1 (2010) 2193.